Article | Open Access

Energy Materials

Thairiyarayar *et al. Energy Mater.* **2026**, *6*, 600053 **DOI:**10.20517/energymater.2026.32

Surface modification and interfacial engineering of Na_3SbS_4 solid electrolytes by polymethylsiloxane-based polymer for high-performance all-solid-state sodium-ion batteries

Celastin Bebina Thairiyarayar[1], Fu-Ming Wang[2,*], Soorathep Kheawhom[3], Jeng-Kuei Chang[3,4], Wei-Ren Liu[1,3,5,*]

Keywords:
Polymer coating, sulfide solid electrolyte, interfacial layer, pore filling, interfacial stability

Citation: Thairiyarayar, C. B.; Wang, F. M.; Kheawhom, S.; Chang, J. K.; Liu, W. R. Surface modification and interfacial engineering of Na_3SbS_4 solid electrolytes by polymethylsiloxane-based polymer for high-performance all-solid-state sodium-ion batteries. *Energy Mater.* **2026**, *6*, 600053. https://dx.doi.org/10.20517/energymater.2026.32

Received: 10 Mar 2026
First Decision: 1 Apr 2026
Revised: 12 Apr 2026
Accepted: 13 May 2026
Published: 22 May 2026

Academic Editor:
Jiazhao Wang
Copy Editor:
Fangling Lan
Production Editor:
Fangling Lan

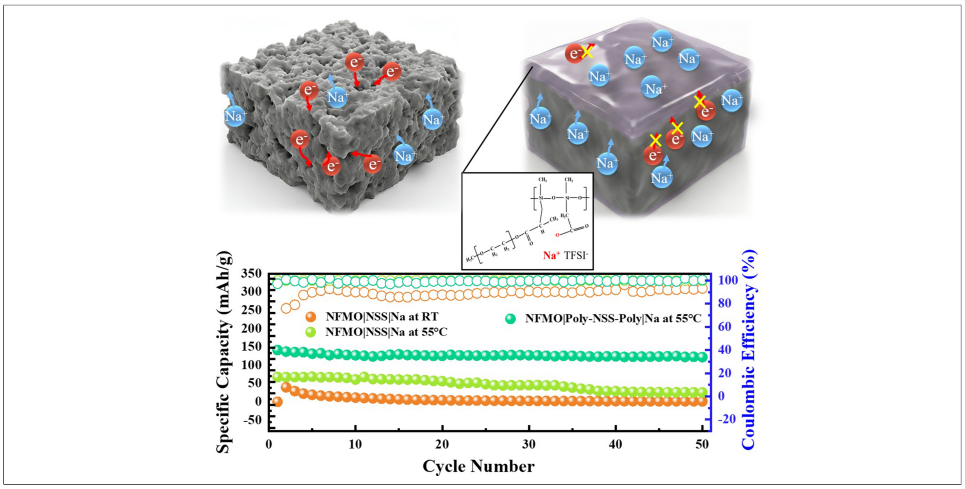

Abstract

All-solid-state batteries are regarded as promising next-generation energy-storage systems due to their potential to achieve energy densities exceeding 400 Wh kg^{-1}. However, their practical implementation remains limited by interfacial instability, non-uniform metal deposition, and continuous electrolyte decomposition during cycling. In this work, a dual-sided polymer coating was introduced onto Na_3SbS_4 solid electrolyte pellets using a siloxane-based sodiated polyelectrolyte (AAM950), combined with sodium bis(trifluoromethylsulfonyl)imide, as an artificial interfacial layer. The conformal coating partially filled surface pores and reduced interfacial gaps, leading to improved solid-solid contact between the electrolyte and electrode. The optimized 7 µL polymer-coated Na_3SbS_4 (NSS) pellet exhibited an ionic conductivity of 0.348 mS cm^{-1} at 55 °C. In addition, the $Na_{2/3}Fe_{1/2}Mn_{1/2}O_2$|Na-AAM950-NSS-Na-AAM950|Na cell delivered an initial discharge capacity of 137.4 mAh g^{-1}, compared with 83.59 mAh g^{-1} for the bare NSS system at

[1]Department of Chemical Engineering, R&D Center for Membrane Technology, Chung Yuan Christian University, Taoyuan 32023, Taiwan.
[2]Sustainable Energy Development Centre, Graduate Institute of Applied Science & Technology, National Taiwan University of Science and Technology, Taipei 10607, Taiwan.
[3]Department of Chemical Engineering, Faculty of Engineering, Chulalongkorn University, Bangkok 10330, Thailand.
[4]Department of Materials Science and Engineering, National Yang Ming Chiao Tung University, Hsinchu 30010, Taiwan.
[5]College of Sustainability, National Tsing Hua University, Hsinchu 30013, Taiwan.

*Correspondence to: Prof. Wei-Ren Liu, Department of Chemical Engineering, R&D Center for Membrane Technology, Chung Yuan Christian University, No. 200, Chung Pei Rd., Chung Li District, Taoyuan 32023, Taiwan. E-mail: wrliu@cycu.edu.tw; Prof. Fu-Ming Wang,

Sustainable Energy Development Centre, Graduate Institute of Applied Science & Technology, National Taiwan University of Science and Technology, Taipei 10607, Taiwan. E-mail: mccabe@mail.ntust.edu.tw

0.02 A g^{-1}, together with a capacity retention of 89.6% and an average Coulombic efficiency of 99.56% over 50 cycles at 55 °C. Although the polymer layer did not substantially increase the intrinsic bulk ionic conductivity of NSS, it effectively stabilized the electrode/electrolyte interface and promoted more homogeneous Na^+ transport during cycling. These findings demonstrate that dual-sided polymer modification provides an effective strategy for improving the practical cycling stability of Na_3SbS_4-based sodium all-solid-state batteries.

INTRODUCTION

Sodium-ion batteries have attracted considerable attention owing to the natural abundance of sodium resources and high theoretical capacity of sodium metal (1,166 mAh g^{-1})[1-3], offering strong potential for high-energy-density storage systems. In this context, sodium all-solid-state batteries (Na-ASSBs) have emerged as a promising alternative because of their enhanced safety arising from the use of non-flammable solid electrolytes. However, despite these advantages, achieving stable and long-term cycling remains a significant challenge. Among the various solid electrolyte candidates, sulfide-based materials have received significant attention because of their high ionic conductivity and relatively soft mechanical properties. Representative examples include Na_3AsS_4 (2.7×10^{-5} S cm^{-1})[4], Na_3BS_3 (1.1×10^{-5} S cm^{-1})[5], Na_3PS_4 (NPS, 3.4×10^{-3} S cm^{-1})[6], and Na_3SbS_4 (NSS, 2.8×10^{-3} S cm^{-1})[7]. However, these sulfide electrolytes are generally limited by their sensitivity to air and, more critically, by interfacial instability during operation. The primary sources of performance degradation are closely associated with interfacial defects such as voids, micro-cracks, and surface roughness, which are generated during pellet compaction. These structural imperfections can act as pathways for electronic leakage, thereby promoting parasitic reactions and accelerating electrolyte degradation[8]. In addition, repeated sodium stripping/plating processes lead to inhomogeneous Na deposition, dendrite formation, and unstable interfacial regions, accompanied by electron penetration into the electrolyte[9]. These combined effects can ultimately result in internal short-circuiting, volumetric expansion, and deterioration of energy density during cycling[10].

On the cathode side, additional instability arises from the intrinsic electrochemical limitations of sulfide electrolytes. Although NSS and NPS exhibit relatively wide electrochemical windows, they undergo decomposition at low potentials (approximately 1.39-2.45 V for NSS and 1.83-1.90 V for NPS)[11,12]. In Na_3SbS_4, mechanical stress coupled with irreversible chemical reactions leads to the formation of Na-Sb binaries, Na_2S, and SbS_3^{3-} species, which act as mixed ionic/electronic resistive interphases[13-15]. Therefore, stabilizing both anodic and cathodic interfaces is essential for achieving a reliable battery performance.

To address these challenges, artificial interfacial engineering strategies have been extensively explored to regulate the electrode/electrolyte interface[16]. These interlayers serve multiple functions, including suppressing direct interfacial reactions, regulating Na^+ flux during stripping/plating, controlling interphase thickness, and reducing interfacial resistance[17]. One common approach involves elemental doping to introduce vacancies or substitutions that facilitate interphase formation, such as NaF- or boride-rich layers through F and B doping[18,19]. However, such doping strategies may adversely affect the mechanical properties of the electrolyte, including Young's modulus and fracture resistance, thereby limiting their practical applicability[17].

Alternatively, surface and interfacial modification strategies have been developed, including polymer coatings, ionic liquid interlayers[20], alucone coatings[21], and membrane-based approaches[22]. Among these, polymer-based coatings are particularly attractive due to their structural flexibility and strong coordination

interactions with Na^+ ions. Functional groups such as C=O, -S, and -F in polymer backbones exhibit high affinity for Na^+, facilitating ion transport while simultaneously improving interfacial contact[23]. Numerous polymer systems, including poly (vinylene carbonate), polyethylene, PVDF-HFP, polyethylene oxide, and polypropylene glycol, have been reported to enhance ionic pathways and interfacial compatibility in solid-state systems[23,24]. Importantly, the effectiveness of polymer interlayers strongly depends on parameters such as the polymer concentration and operating temperature. A lower polymer concentration can reduce the viscosity, enhance wettability, and improve pore filling, thereby facilitating ion transport[9]. In addition, elevated temperatures significantly enhance Na^+ mobility by promoting grain-boundary diffusion within the solid electrolyte and activating segmental motion in polymer chains, enabling efficient ion hopping through coordinated polymer-salt networks[20].

Recent studies on Na_3SbS_4-based systems have further highlighted the role of polymer interlayers in regulating electrode/electrolyte interfacial behavior. Pristine Na_3SbS_4 exhibits an ionic conductivity of approximately 3.1×10^{-4} S cm^{-1} at room temperature, whereas polymer-modified systems such as PEG-PPG-PEG (PPP)/sodium bis(trifluoromethylsulfonyl)imide (NaTFSI) composites show slightly lower conductivity values of 1.9×10^{-4} S cm^{-1} together with increased activation energy (0.20-0.31 eV)[25]. These results indicate that polymer incorporation does not necessarily enhance the intrinsic bulk ionic transport properties of the electrolyte. Instead, the primary effect of the polymer interlayer is associated with interfacial stabilization during electrochemical cycling. For example, bare NSS cells exhibit a substantial increase in electrode/electrolyte interfacial resistance from 318.2 to 6,475 Ω because of the continuous formation of decomposition products such as Na_3Sb and Na_2S, whereas polymer-modified systems effectively suppress this resistance growth and maintain more stable cycling behavior[26,27]. Similarly, ionic-liquid-based interlayers containing $TFSI^-$ anions, such as Pyr_{14}TFSI-NGE (Na_3SbS_4-glassfiber electrolyte) systems, have demonstrated enhanced anti-dendrite performance and stable cycling over extended periods at 0.1 mA cm^{-2}[20]. Wang *et al.* further reported that incorporating BMTFSI (1-butyl-1-methyl pyrrolidinium bis (trifluoro methyl sulfonyl) imide) ionic liquid into PVDF (Poly (vinylidene fluoride)) polymer improved void filling and achieved ionic conductivity up to 3.18 mS cm^{-1} with low additive loading[28]. In addition, PYR/NaTFSI interlayers have demonstrated a high specific capacity (300 mAh g^{-1}) in FeS_2||Na systems, attributed to the formation of NaF and CF_3-containing interfacial species during cycling[29]. Despite these advances, the development of polymer systems that simultaneously provide effective interfacial contact, chemical compatibility, and stable electrochemical performance in sulfide-based Na-ASSBs remains limited.

Herein, we report the first application of a siloxane-based sodiated polyelectrolyte interfacial layer for Na_3SbS_4 solid electrolytes. The polymer is based on a poly (dimethyl siloxane) backbone functionalized with ethylene glycol methyl ether, methacrylate, and acrylic acid groups, providing enhanced mechanical flexibility, interfacial adhesion, and Na^+ coordination capability[30]. The incorporation of NaTFSI increases Na^+ concentration and facilitates ion transport across the solid electrolyte/polymer/electrode interfaces. Furthermore, operation at 55 °C induces a semi-glassy polymer state with reduced viscosity, improving interfacial wetting, filling surface defects, and enhancing electrochemical performance under practical conditions.

EXPERIMENTAL

Preparation of Na_3SbS_4 solid electrolyte pellet

The Na_3SbS_4 (NSS) solid electrolyte was synthesized according to our previous report[31]. NSS pellets were prepared from a ball-milled mixture of Na_2S (90+% purity, Alfa Aesar, Karlsruhe, Germany), Sb_2S_3 (98% purity, Alfa Aesar, Germany), and S (99.9% purity, Sigma-Aldrich, Schnelldorf, Germany) in a 3:1:2 ratio. The precursor mixture was ball-milled at 560 rpm for 20 h, followed by thermal treatment at 250 °C for 12 h, as illustrated in Figure 1. The resulting powder was pelletized under a pressure of 360 MPa in an argon atmosphere.

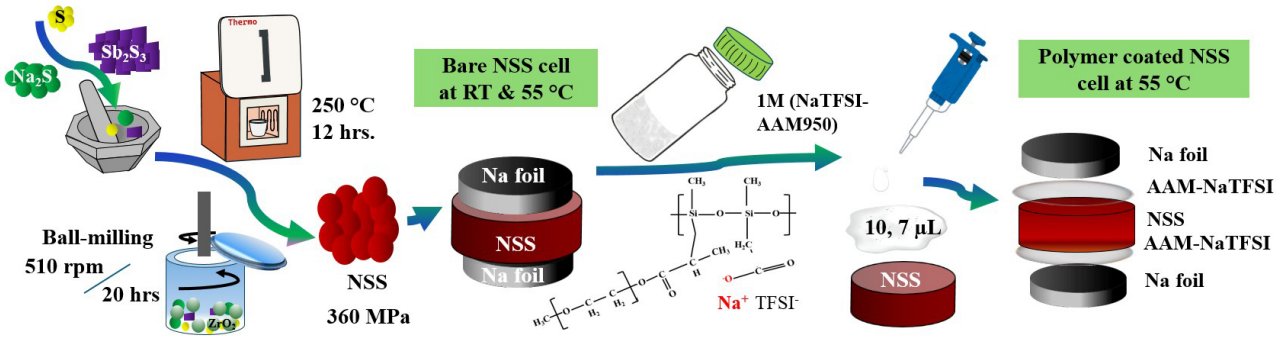

Figure 1. Flow chart of dual side AAM950 polymer coating on the pellet of prepared Na_3SbS_4 (NSS) solid electrolyte.

Surface modification of NSS pellet-AAM950 polymer coating

The sodiated polyelectrolyte was prepared as described in our previous report[30]. AAM950 polymer, a poly (dimethyl siloxane)-based functionalized polymer, was combined with 1 M bis(trifluoromethylsulphonyl)imide sodium salt (NaTFSI, ≥ 99.5%, Aladdin). NaTFSI was first dissolved in a small amount of dimethyl carbonate (DMC, 99%, Thermos scientific) and ground in an agate mortar for a minute to obtain a concentrated, clear solution. Subsequently, AAM950 polymer was added and mixed until a homogeneous, viscous gel was obtained. A defined volume (5, 7, 10 and, 12 µL) of the gel was deposited onto the surface of the NSS pellet using a pipette and uniformly spread with a spatula, as shown in Figure 1, inside a glove box (H_2O < 0.5 ppm, O_2 < 0.5 ppm). The DMC solvent evaporated naturally at room temperature within 2-3 min without external heating, leaving behind a uniform polymer coating layer.

Assembly of symmetric sodium all-solid-state cells

Symmetric Na||Na cells were assembled using Na metal foils with an 8 mm diameter (Alfa Aesar) placed on both sides of the 1 M NaTFSI-AAM950/NSS/NaTFSI-AAM950 pellet, as shown in Figure 1. Stainless steel spacers and springs were incorporated into CR2032-type coin cells, and the assembled cells were compressed at 210 MPa to maintain stable interfacial contact.

Fabrication of asymmetric half-cells

Asymmetric half-cells were assembled using $Na_{2/3}Fe_{1/2}Mn_{1/2}O_2$ (NFMO, SKSTC) as the cathode. A slurry comprising NFMO, Poly (vinylidene fluoride) (PVDF) binder, and Super P conductive carbon in an 8:1:1 weight ratio was prepared in N-methyl-2-pyrrolidone (NMP) and stirred overnight to ensure homogeneity. The slurry was cast onto aluminum foil, vacuum-dried at 120 °C for 9 h, and punched into 10 mm diameter electrodes[31]. Sodium metal foil served as the anode, with the AAM950-NaTFSI-coated NSS solid electrolyte positioned between the electrodes in a sandwich configuration. The assembled cells were compacted at 210 MPa and handled entirely inside an argon-filled glovebox (LABstar, MBraun, Germany; H_2O and O_2 < 0.5 ppm).

Material characterizations

Raman spectra were obtained using a Raman spectrometer system provided by BWTEK (model BAC102-532E, USA). Fourier transform infrared (FT-IR) spectra were obtained to determine functional groups and bonding through a Bruker Vertex 70 model FT-IR spectrometer (Germany). Morphological and elemental analyses were performed using a field-emission scanning electron microscope (FE-SEM; model JSM-7600F, JEOL, Japan) interfaced with an energy-dispersive spectrometer (EDS; X-MAX, Oxford Instruments, UK). The valence-state analysis of elements in the material was performed using X-ray photoelectron spectroscopy (XPS; K-Alpha, Thermo Scientific, Waltham, MA, USA).

Electrochemical measurements

Electrochemical characterization was performed using a Biologic SP-200 potentiostat (France) under the same conditions as reported previously[31]. Electrochemical impedance spectroscopy (EIS) was performed on pressed electrolyte pellets (10 mm diameter, 70 mg) under a pressure of 360 MPa, over a frequency range of 7 MHz to 10 mHz with an AC amplitude of 10 mV. The ionic conductivity (σ) was calculated using Equation (1)[29]:

$$\sigma = L/(R \cdot A) \quad (1)$$

Here, L is the pellet thickness, R is the total resistance obtained from Nyquist plots, and A is the cross-sectional area of the pellet. The cross-sectional area (A) was 0.785 cm^2 for a pellet diameter of 10 mm. Stripping/plating, critical current density (CCD), DC polarization, and cyclic voltammetry (CV) measurements were conducted using Na||Na symmetric cells. The stripping/plating tests were performed at a current density of 0.1 mA cm^{-2} with 1 h charge/discharge cycles, while CCD measurements were carried out in the range of 0.1-1.5 mA cm^{-2}. DC polarization was performed by applying a constant bias of 500 mV, and CV measurements were conducted at a scan rate of 0.2 mV s^{-1}. Linear sweep voltammetry (LSV) was carried out using Na|stainless steel (SS) cells at a scan rate of 0.1 mV s^{-1}. Half-cell tests of NFMO|SE|Na cells were performed within a voltage window of 2.0-3.8 V *vs.* Na/Na^+, and galvanostatic charge/discharge measurements (NEWARE, Battery testing system- China) were conducted at room temperature (RT) and 55 °C.

RESULTS AND DISCUSSION

To investigate the structural interactions between the NSS solid electrolyte and the AAM950 polymer coating, Raman and FTIR analyses were performed, as shown in Figure 2. The Raman spectra in Figure 2A confirm the successful incorporation of NaTFSI into the AAM950 polymer and its subsequent deposition onto the NSS pellet surface. The AAM950-NaTFSI spectrum exhibits the characteristic NaTFSI vibration at 750 cm^{-1}, along with a broad amorphous polymer feature centered around 2,800 cm^{-1}. In addition, the broad band observed in the 1,500-2,000 cm^{-1} region suggests strong interactions between the polymer and NaTFSI salt within the coating layer. Importantly, despite the introduction of the polymer layer, the characteristic $[SbS_4]^{3-}$ tetrahedral vibrations at 410, 389, and 368 cm^{-1} remained present in both pristine NSS[32] and polymer-coated NSS (expanded view at 318-500 cm^{-1}) samples, indicating that the polymer coating preserves the crystalline framework of the Na_3SbS_4 solid electrolyte[25].

To further examine the interfacial interactions and chemical environment, FTIR spectra were analyzed, as shown in Figure 2B. The spectra reveal a uniform distribution of NaTFSI within the AAM950 polymer coating together with a clear interaction between the polymer and NSS surface. Pristine NaTFSI exhibits characteristic asymmetric and symmetric SO_2 stretching modes of the $TFSI^-$ anion at 1,336 and 1,141 cm^{-1}, respectively, along with CF_3 stretching vibrations at 1,233 and 1,063 cm^{-1}[33-37]. Imide S-N-S vibrations are observed at 800 and 745 cm^{-1}[34,36,37]. In the NSS spectrum, characteristic ν(Sb-S) stretching modes of the SbS_4^{3-} tetrahedra appear at 570.8 and 513.9 cm^{-1}[33].

In addition, weak features between 1,386 and 1,067 cm^{-1} were attributed to slight surface oxidation during sample handling. Hydration-related bands at 1,642 and 1,617 cm^{-1}, together with broad O-H stretching above 3,200 cm^{-1}, indicate the presence of lattice-bound water associated with Schlippe's salt ($Na_3SbS_4 \cdot 9H_2O$)[35], highlighting the sensitivity of this material. Furthermore, the AAM950 is confirmed as a silicon-based polymer with a siloxane backbone, characterized by Si-O-Si stretching near 1,100 cm^{-1} and Si-H vibrations at 2,160 cm^{-1}[37]. The polymer side chains consist of poly (ethylene glycol), identified by C-O-C stretching

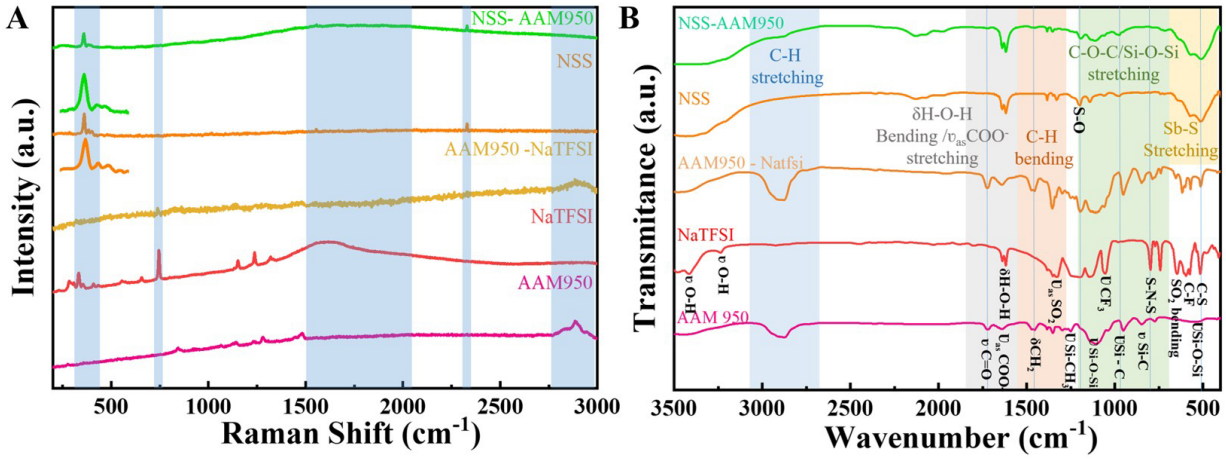

Figure 2. (A) Raman spectra (Inset: Enlarged view of 318-500 cm^{-1}) and (B) FTIR spectra of individual AAM950 polymer components before and after coating on the NSS surface.

around 1,070 cm^{-1} and aliphatic C-H stretching near 2,900 cm^{-1}[22], while carboxylate groups are indicated by a band near 1,617 cm^{-1}[22]. Upon incorporation of NaTFSI, sodium ions coordinate with ether oxygen atoms and carboxylate groups along the polymer chains, leading to broadening of the Si-O-Si band near 1,100 cm^{-1}, which suggests strong polymer-ion interactions within the coating. Notably, the retention of Sb-S vibrations in the 514-570 cm^{-1} range confirms that the crystalline framework of NSS remains intact after polymer coating. Moreover, overlapping bands near 1,617 cm^{-1} indicate strong interfacial interactions between the inorganic NSS surface and the organic polymer layer. This interfacial coupling is expected to facilitate Na^+ transport across the inorganic-organic boundary, thereby contributing to improved electrochemical performance.

To correlate these spectroscopic findings with morphological evolution, SEM analysis was performed. The SEM image of the pristine NSS pellet, as shown in Figure 3A at a 1 μm scale, reveals a porous and agglomerated morphology characterized by numerous interparticle voids. These structural features can promote localized electronic pathways and poor interfacial contact, leading to interfacial instability during electrochemical cycling. By comparison, the polymer-coated sample shown in Figure 3B exhibits a significantly denser and more homogeneous surface morphology. The porous structure and interparticle voids are effectively suppressed after coating with 7 μL of AAM950-NaTFSI polymer electrolyte. The polymer layer forms a continuous and conformal coating, as further confirmed by the corresponding optical image. This conformal coating establishes a continuous interfacial layer that can reduce direct electronic pathways while maintaining ionic transport, thereby improving interfacial stability.

To further verify the compositional uniformity of the coating layer, SEM-EDS elemental mapping was performed as shown in Figure 4. The elemental maps of pristine NSS [Figure 4A] show uniform distributions of Na, Sb, and S, confirming the homogeneous nature of the Na_3SbS_4 electrolyte. After polymer coating, the sample in Figure 4B exhibits additional Na, S, and N signals originating from NaTFSI, together with Si, O, and C signals from the AAM950 polymer matrix. The homogeneous elemental distribution confirms the successful incorporation of NaTFSI within the polymer framework and its uniform coverage over the NSS surface.

Electrochemical impedance spectroscopy (EIS) measurements were performed to evaluate the influence of polymer coating on ionic transport and interfacial behavior, as presented in Figure 5A (Inset: Equivalent circuit). The pristine NSS electrolyte exhibited an ionic conductivity of 3.11×10^{-4} S cm^{-1} at room temperature[3]

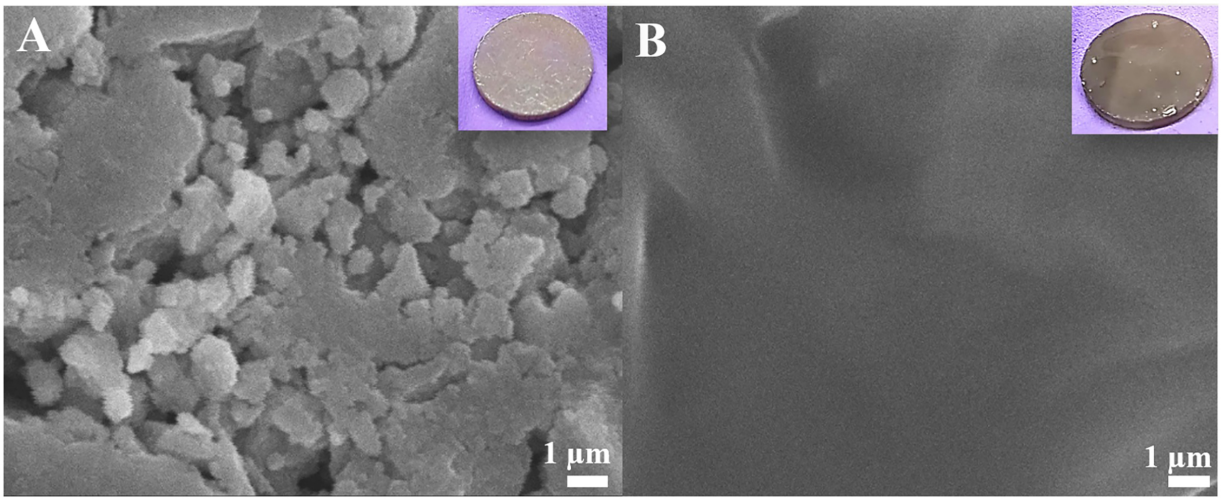

Figure 3. Top-view SEM images and corresponding optical photographs of (A) Na_3SbS_4 (NSS) and (B) AAM950 polymer-coated NSS pellets.

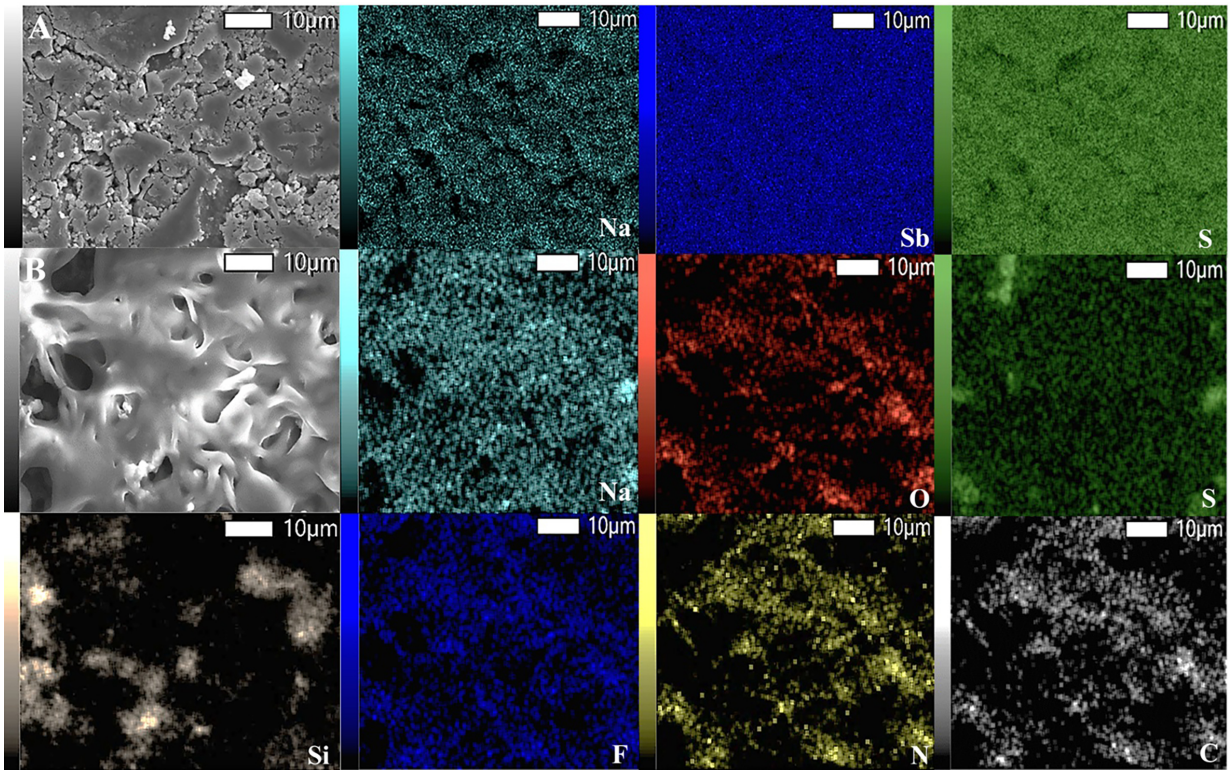

Figure 4. SEM-EDS elemental mappings of (A) pristine Na_3SbS_4 showing Na, Sb, and S distributions, and (B) AAM950 polymer-coated NSS showing Na, O, S, Si, F, N, and C distributions.

whereas the 10 and 7 µL polymer-coated samples showed reduced ionic conductivities because of the additional polymer transport layer, as summarized in Table 1. At elevated temperature (55 °C), the overall resistance decreased substantially because of reduced polymer viscosity and enhanced segmental mobility within the polymer matrix. Among all coating conditions, the 7 µL-coated sample exhibited the lowest total resistance at 55 °C together with the highest ionic conductivity of 3.48×10^{-4} S cm^{-1}. In contrast, the 10 µL-coated sample exhibited slightly higher resistance because the thicker polymer layer hindered Na^+

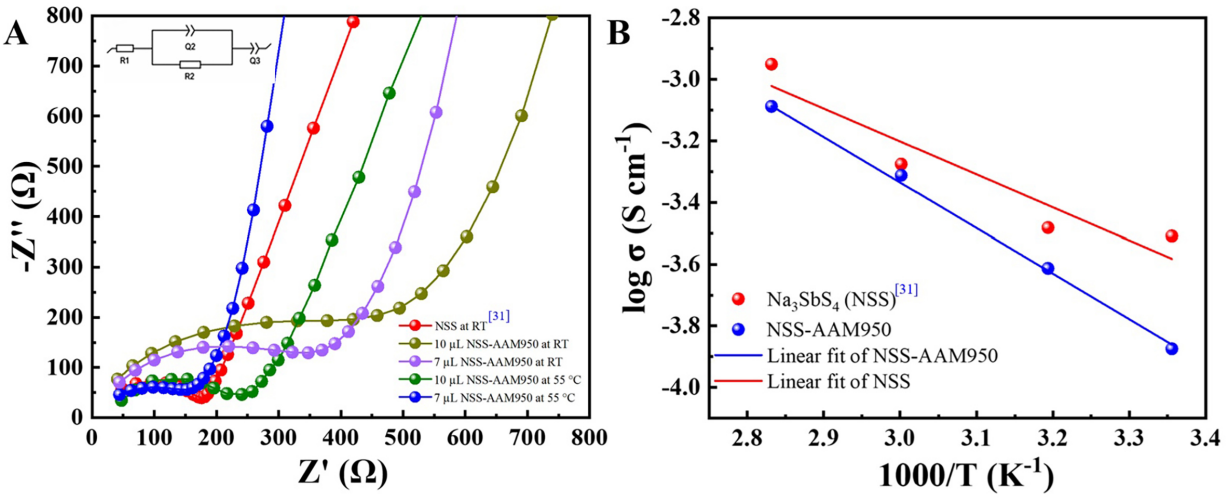

Figure 5. Electrochemical characterization of NSS electrolytes with and without polymer coating. (A) Nyquist plots of NSS pellets coated with different volumes of AAM950 polymer (Inset: Equivalent circuit). Bare NSS data were reproduced from Ref.[31] for comparison. (B) Arrhenius plots showing the temperature-dependent ionic conductivity of pristine NSS and 7 µL AAM950-coated NSS from 25 to 80 °C.

Table 1. Ionic conductivity values of pristine Na_3SbS_4 (NSS) and NSS pellets coated with different volumes of AAM950-NaTFSI polymer electrolyte

Sample (NSS-poly)	$R_{tot} = (R_1 + R_2)$ (Ω)	L (µm)	Ionic conductivity ($\times 10^{-3}$ S cm^{-1})
NSS	175.4	430	0.31
10 µL at RT	469.15	470	0.109
7 µL at RT	367	450	0.156
10 µL at 55 °C	208.6	470	0.27
7 µL at 55 °C	172.2	450	0.348

RT: Room temperature.

transport. The Nyquist profile of the 5 µL-coated sample displayed partially separated semicircle features, suggesting incomplete polymer coverage and non-uniform electrolyte/electrode contact. Meanwhile, the 12 µL-coated sample shown in Supplementary Figure 1 exhibited a broader depressed semicircle associated with excessive polymer thickness and slower ion transport. The extracted ionic conductivity values are summarized in Supplementary Table 1. Overall, the impedance response was dominated by a depressed semicircle, indicating overlapping ionic transport contributions from both NSS and the polymer layer. Therefore, the analysis mainly focuses on total resistance rather than complete separation of individual components. These observations suggest that the polymer coating primarily improves interfacial conformity and stabilizes Na^+ transport pathways rather than significantly enhancing the intrinsic bulk ionic conductivity of NSS. The temperature-dependent ionic conductivity follows the Arrhenius relationship[31], according to Equation (2):

$$\sigma = A \exp(-E_a/kT) \quad (2)$$

The ionic conductivity of the 7 µL AAM950-NaTFSI-coated NSS increased from 1.56×10^{-4} S cm^{-1} at 25 °C to 8.17×10^{-4} S cm^{-1} at 80 °C, confirming thermally activated Na^+ transport behavior, as shown in Figure 5B. For comparison, pristine NSS exhibited ionic conductivity increasing from 3.11×10^{-4} S cm^{-1} at 25 °C to 1.12×10^{-3} S cm^{-1} at 80 °C[31]. The polymer-coated sample exhibited a higher activation energy of 0.30 eV

compared with pristine NSS (0.21 eV), indicating that the polymer layer introduces an additional energy barrier for Na^+ migration. Although the polymer coating slightly reduces bulk ionic conductivity, it forms a conformal interfacial layer while partially filling surface pores within the NSS pellet. This interfacial modification helps maintain electrode/electrolyte contact and supports more stable cell operation, especially at 55 °C.

Symmetric Na||Na cells were subsequently evaluated through stripping/plating measurements at 0.1 mA cm^{-2} to investigate interfacial stability, as shown in Figure 6A. The pristine NSS electrolyte initially exhibited a low overpotential of approximately 0.025 V; however, the polarization rapidly increased to nearly 0.5 V, and the cell failed after 10 cycles. This unstable behavior reflects poor interfacial contact together with continuous interfacial degradation during repeated Na plating/stripping. The 7 μL AAM950-NaTFSI-coated NSS maintained a comparatively stable overpotential of approximately 0.08 V for more than 40 cycles. This improved electrochemical behavior suggests enhanced interfacial conformity and more uniform Na deposition enabled by the polymer interlayer. The corresponding impedance evolution during cycling is presented in Figure 6B (Inset: Equivalent circuit). The polymer-coated electrolyte maintained relatively stable impedance behavior throughout cycling, while the interfacial resistance (R_3) decreased slightly from 1,500.3 to 1,357 Ω during the initial cycling process. This behavior may be associated with improved physical contact and interface wetting between Na metal and the polymer-coated electrolyte during repeated stripping/plating. Critical current density (CCD) measurements performed at 55 °C are shown in Supplementary Figure 2. For pristine NSS, the voltage profile remained relatively stable at low current density but exhibited abrupt failure at 0.65 mA cm^{-2}, indicating internal short-circuiting caused by unstable Na deposition. In addition, the fluctuating voltage response observed at 55 °C compared with the smoother room-temperature behavior suggests intensified interfacial reactions and non-uniform Na plating at elevated temperature. Meanwhile, the 7 μL AAM950-NaTFSI-coated NSS exhibited gradual polarization increase from 0.1 to 0.9 V across the tested current-density range of 0.1-1.5 mA cm^{-2} without abrupt voltage collapse. This behavior indicates improved tolerance toward high-current operation together with delayed short-circuit formation arising from more homogeneous Na deposition and reduced localized current concentration.

To further clarify the interfacial evolution, EIS measurements were conducted before and after CCD testing, as shown in Supplementary Figure 3 (Inset: Equivalent circuit; enlarged high-frequency region). The extracted fitting parameters are summarized in Supplementary Table 2. After CCD testing, the pristine NSS cell exhibited abnormal impedance behavior associated with internal short-circuiting and cell failure. In contrast, the polymer-coated sample retained measurable impedance behavior after cycling, although the interfacial resistance still increased because of continued interphase evolution during high-current operation. Thus, the coating does not eliminate interfacial reactions, but it slows their progression and preserves a more functional interface during high-current operation. Linear sweep voltammetry (LSV) measurements shown in Figure 6C were performed to evaluate the electrochemical behavior of the NSS electrolyte. The pristine NSS measured at room temperature exhibited a sharp increase in current near 2.6 V, indicating the onset of oxidative decomposition. The polymer-coated NSS measured at 55 °C exhibited significantly suppressed current response throughout the measured voltage range up to 7 V. Although direct comparison is limited because of the different testing temperatures, the reduced current response suggests moderated oxidative reactions under the tested conditions.

The sodium-ion transference number was calculated using Equation (3)[38],

$$t_{Na}^{+} = \frac{I_{SS}}{I_0} \times \frac{(\Delta V - I_0 R_0)}{(\Delta V - I_{SS} R_{SS})} \quad (3)$$

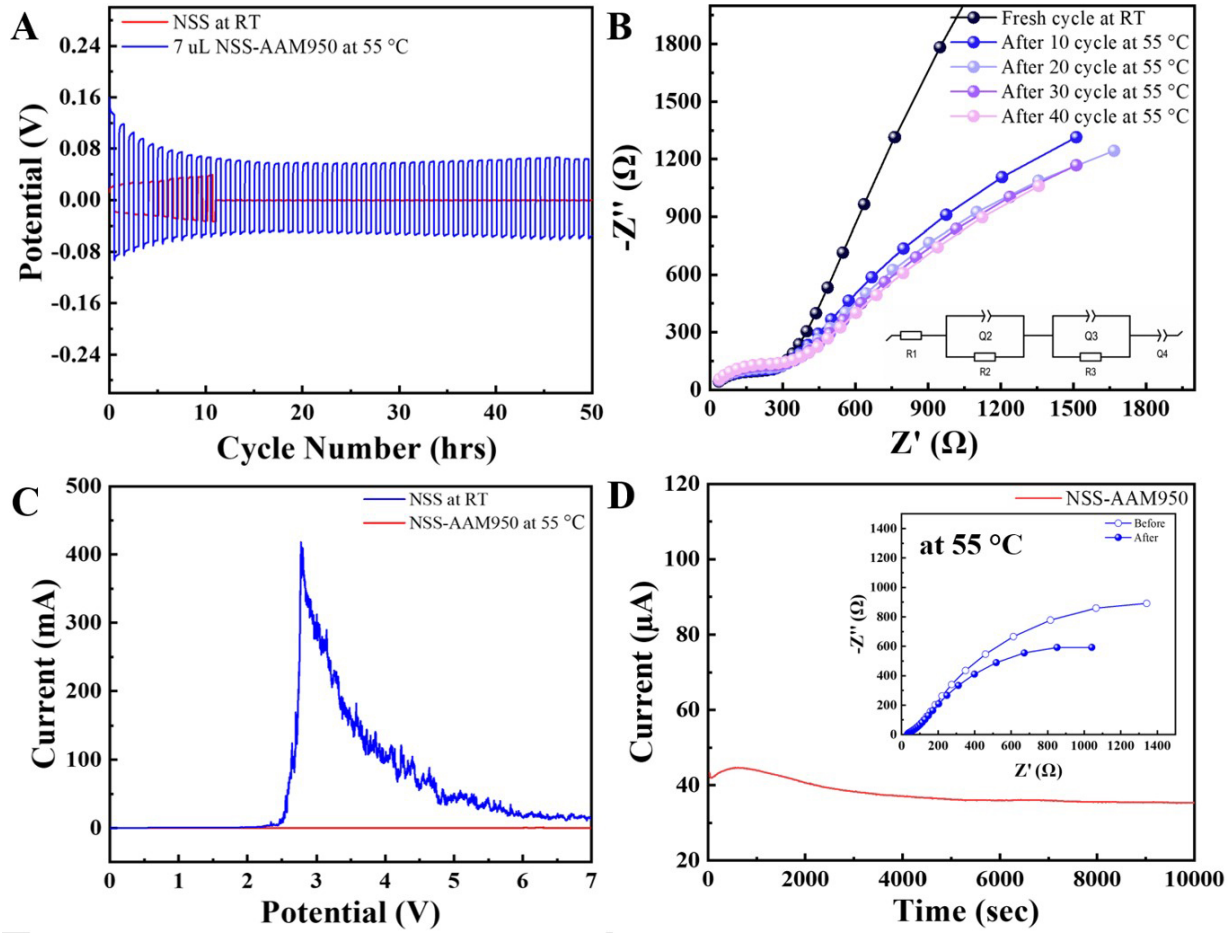

Figure 6. (A) Stripping/plating profiles at 0.1 mA cm^{-2} and (B) corresponding Nyquist plots of 7 μL AAM950-NSS-AAM950 at 55 °C (Inset: Equivalent circuit). (C) Linear sweep voltammetry (LSV) curves of pristine NSS at RT and 7 μL AAM950-NSS-AAM950 at 55 °C measured at 0.1 mV s^{-1}. (D) DC polarization profile at 500 mV (Inset: Nyquist plot).

The electrolyte properties were further evaluated through direct current polarization and impedance analysis [Figure 6D]. The 7 μL polymer-coated cell exhibited an initial current (I_0) of 47.80 μA, which stabilized at 36 μA. The corresponding initial and steady-state interfacial resistances obtained from the Nyquist plots were 1,342 and 1,041 Ω, respectively. Based on these values, the Na^+ transference number (t_{Na^+}) was calculated to be 0.74. This relatively high t_{Na^+} value indicates efficient Na^+ transport within the polymer-modified system. Together with the improved CCD performance, these observations suggest that the polymer layer facilitates ion transport and promotes more uniform Na^+ flux at the interface, despite gradual interfacial resistance evolution during prolonged cycling.

The interfacial behavior of symmetric Na||Na cells was further investigated using cyclic voltammetry over a potential range of -0.5 to 0.5 V, together with impedance analysis (Inset: Equivalent circuit), as shown in Figure 7, and the corresponding resistance values obtained from equivalent circuit fitting are presented in Table 2. For pristine NSS at room temperature [Figure 7A], the cathodic current decreased significantly from -0.139 mA in the first cycle to -0.017 mA by the fifth cycle, indicating a progressive loss of electrochemical activity caused by interfacial degradation. Correspondingly, the impedance response [Figure 7C] exhibited continuous resistance increase, where R_2 increases from 694.31 to 2,798 Ω and R_3 increases from 1,725 to 4,870 Ω, reflecting the formation of a highly resistive interfacial region and poor charge-transfer kinetics. Meanwhile, the polymer-coated NSS at 55 °C [Figure 7B] exhibited more stable electrochemical behavior,

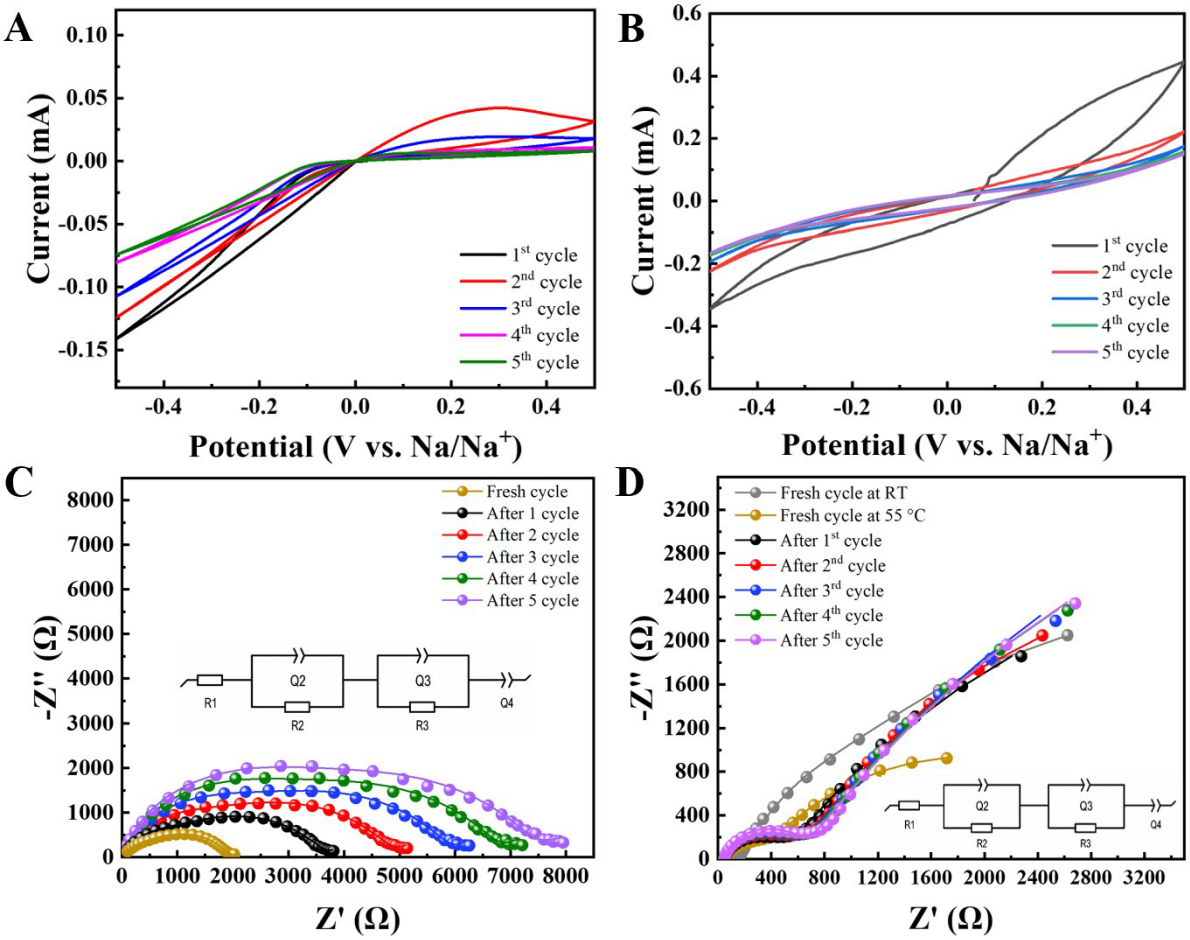

Figure 7. (A) Cyclic voltammetry and (C) Nyquist plots of pristine NSS at RT (Inset: Equivalent circuit), (B) Cyclic voltammetry and (D) Nyquist plots of 7 µL of AAM950-NSS-AAM950 at 55 °C (Inset: Equivalent circuit).

with the cathodic current varying from 0.33 to 0.162 mA over five cycles. The Nyquist plots [Figure 7D] showed a different resistance evolution, where R_1 remains relatively constant from 46.08 to 45.38 Ω, R_2 increases moderately from 302.03 to 555.77 Ω, and R_3 decreases from 3,102 to 826.75 Ω. The decrease in R_3 during initial cycling suggests improved interfacial contact and activation of the interface, likely due to better wetting and conformal contact provided by the polymer layer. However, this behavior should be interpreted as interfacial adaptation rather than complete suppression of degradation. Overall, the CV-EIS results confirm that the polymer layer promotes interfacial activation and maintains a more stable contact geometry during repeated Na plating/stripping.

Electrochemical impedance spectroscopy was further performed before cycling and after 50 cycles at 55 °C to evaluate interfacial evolution in NFMO|SE|Na cells, as shown in Figure 8A and B, with the fitted equivalent circuit presented in the inset. The high-frequency regions of Figure 8A and B are provided in Supplementary Figure 4A and B. Before cycling, both systems show lower initial resistance at 55 °C than at room temperature. For the bare NSS cell, the high-frequency intercept appears to decrease from approximately 49.8 Ω at RT to around 12.3 Ω at 55 °C, with a clear reduction in the semicircle size. For the polymer-coated NFMO|Poly-NSS-Poly|Na cell, the initial resistance is higher at RT, with the intercept near 74.9 Ω, while at 55 °C it shifts to about 40 Ω, indicating enhanced ionic transport and improved interfacial contact at elevated temperature. After cycling at 55 °C, the impedance evolution shows a clear difference between the two systems. The bare NSS cell exhibits a substantial increase in charge-transfer resistance from

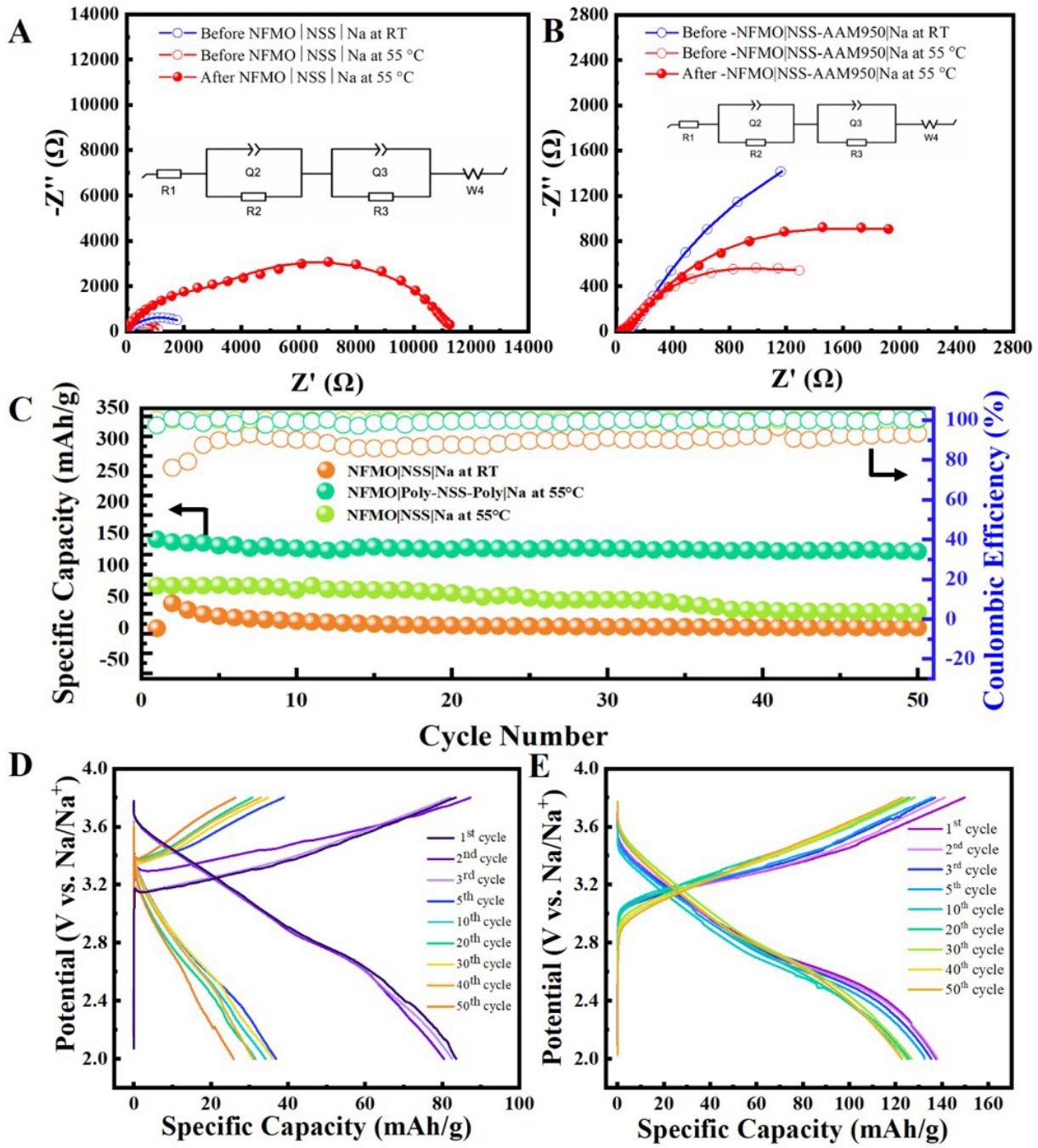

Figure 8. Nyquist impedance spectra before and after 50 electrochemical cycles of NFMO|SE|Na cells at 0.02 A g^{-1}: (A) pristine NSS and (B) 7 µL AAM950-NSS-AAM950 at 55 °C (Inset: Equivalent circuit). (C) Cycling performance of NFMO|NSS|Na and NFMO|7 µL AAM950-NSS-AAM950|Na cells. (D and E) Corresponding galvanostatic charge/discharge profiles.

150 to approximately 13,000 Ω after 50 cycles, indicating severe interfacial degradation and the formation of a highly resistive interphase. In comparison, the polymer-coated cell shows a moderate increase in resistance from 550 to 950 Ω under the same conditions, suggesting that interfacial degradation still occurs but is significantly mitigated compared to the bare system. The electrochemical performance shown in Figure 8C is consistent with this impedance behavior. The NFMO|NSS|Na cell delivers an initial discharge capacity of 83.59 mAh g^{-1} at 55 °C and 0.02 A g^{-1}, with the Coulombic efficiency decreasing to 44.6% after 50 cycles. The corresponding voltage profiles in Figure 8D within the range of 2.0 to 3.8 V, show irregular shapes,

Table 2. Comparison of charge-transfer resistance values derived from cyclic voltammetry measurements

Samples	Cycle number	R_1 (Ω)	R_2 (Ω)	R_3 (Ω)
NSS at RT	Fresh cycle	32.3	694.31	1,725
	1 cycle	33.68	523.9	3,099
	2 cycle	25	1,273	3,433
	3 cycle	19.35	1,731	4,253
	4 cycle	18.04	2,558	4,326
	5 cycle	15.75	2,798	4,870
NaTFSI-AAM-NSS at 55 °C	Fresh cycle	46.08	302.03	3,102
	1 cycle	47.77	409.05	1,623
	2 cycle	47.23	506.29	1,062
	3 cycle	45.94	519.87	943.33
	4 cycle	45.97	549.3	891.03
	5 cycle	45.38	555.77	826.75

NSS: Na_3SbS_4; NaTFSI: sodium bis(trifluoromethylsulfonyl)imide; RT: room temperature.

increasing polarization, and widening hysteresis during cycling, indicating unstable interfacial processes and poor reversibility. On the other hand, for the polymer-coated cell, the initial charge and discharge capacities are 149.7 and 137.4 mAh g^{-1}, respectively, with an average Coulombic efficiency of 99.56% over 50 cycles. The voltage profiles in Figure 8E are smoother with reduced polarization over the same voltage range. A slight decrease in capacity is observed during the initial cycles, followed by relatively stable performance up to 50 cycles. This improved cycling behavior correlates with the moderate increase in interfacial resistance, indicating that although degradation processes are not eliminated, they are effectively suppressed and stabilized during cycling. Therefore, these results collectively demonstrate that the polymer coating improves interfacial contact and moderates the rate of interfacial resistance growth, rather than preventing degradation entirely.

The chemical and morphological evolution of the 7 μL NaTFSI-AAM950 polymer coating on the NSS solid electrolyte is presented in Figure 9. For comparison, the polymer-coated surface shown in Figure 9A is displayed again alongside the pristine NSS surface shown in Figure 3A. Before cycling, SEM imaging [Figure 9A] revealed a smooth, dense, and homogeneous polymer layer, indicating effective surface coverage and good film-forming behavior. The corresponding Na 1s spectrum [Figure 9B] exhibited two sodium environments, attributed to NaTFSI (1,071.8 eV) and the underlying NSS (1,070.8 eV). The Sb 3d and O 1s spectra shown in Figure 9C display characteristic Sb $3d_{5/2}$ and Sb $3d_{3/2}$ peaks at 529.5 and 538.8 eV, respectively, together with C-O (533.5 eV) and C=O (531.8 eV) contributions associated with the polymer matrix. After 50 electrochemical cycles, the surface morphology [Figure 9D] exhibited crystalline features while remaining continuous without large-scale structural degradation. This observation indicates that although interfacial reactions occurred during cycling, the overall integrity of the coating layer was maintained. The post-cycling Na 1s spectrum [Figure 9E] was dominated by a peak assigned to NaF (1,071.8 eV), together with an additional contribution at 1,071.0 eV associated with Na_2O and residual NSS components. In the O 1s spectrum [Figure 9F], the emergence of a peak at 531.2 eV is attributed to oxidized antimony species (Sb-O), accompanied by an increased contribution near 528.5 eV corresponding to Na_2O. These results indicate the formation of interfacial decomposition products during cycling, rather than a fully stable or inert interface. Nevertheless, the presence of NaF and Na_2O, along with the preserved structural continuity of the coating layer, suggests the formation of a relatively stable and ionically conductive interphase capable of moderating interfacial degradation.

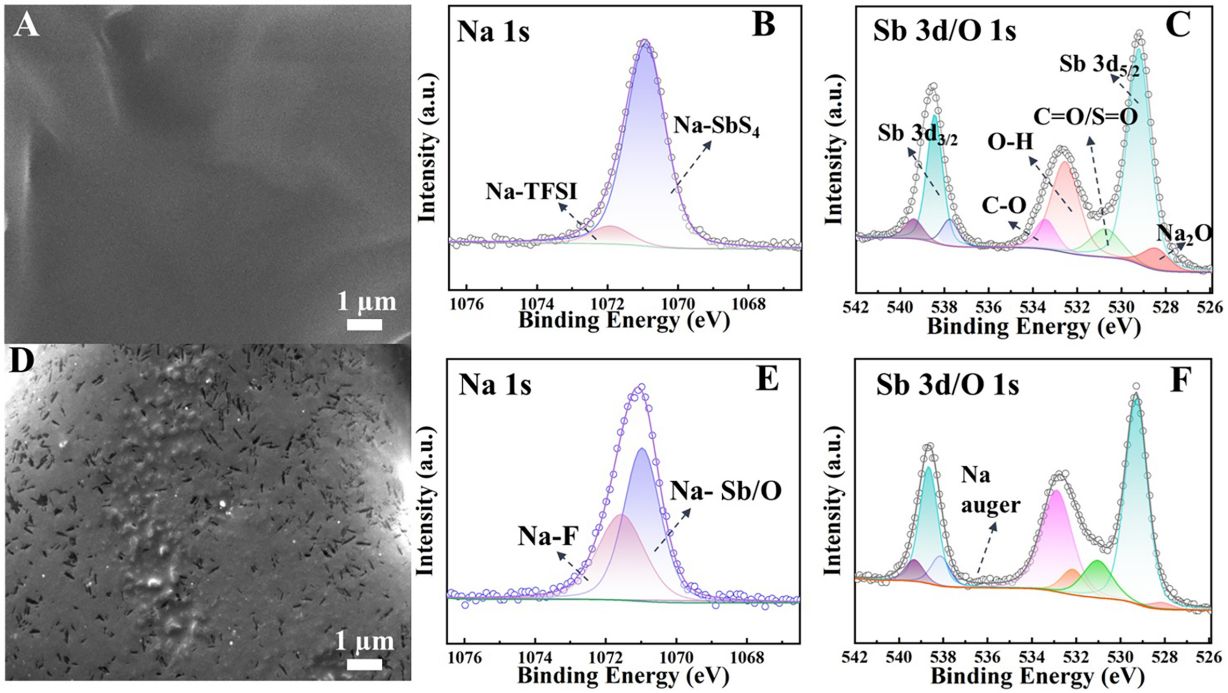

Figure 9. Top-view SEM and XPS analysis of the AAM950-coated NSS solid electrolyte before and after cycling. (A) SEM image of the polymer-coated surface is shown again for better comparison with the pristine NSS in Figure 3A. XPS spectra before cycling include (B) Na 1s and (C) Sb 3d/O 1s. After 50 electrochemical cycles, (D) top-view SEM shows the morphological evolution, while XPS spectra of (E) Na 1s and (F) Sb 3d/O 1s reveal chemical changes at the interface in the disassembled NFMO|7 μL AAM950-NSS-AAM950|Na cell tested at 55 °C.

To evaluate the interfacial morphology and chemical evolution, Figure 10 presents cross-sectional SEM images together with S 2p and F 1s XPS spectra obtained before and after cycling. The initial cross-section [Figure 10A] reveals that the 7 μL polymer layer possesses an approximate thickness of 8.7 μm and forms a continuous contact with the NSS surface. This observation suggests that the polymer is not merely a superficial coating but partially penetrates into the near-surface region of the porous electrolyte, thereby enhancing interfacial conformity. The initial S 2p spectrum [Figure 10B] shows contributions from $TFSI^-$ species at 169.0 eV and the characteristic Sb-S-Na environment at 161.2 eV. The corresponding F 1s spectrum [Figure 10C] displays a dominant C-F_3 signal at 688.6 eV, confirming the presence of intact NaTFSI within the polymer layer before cycling. After 50 electrochemical cycles, the cross-sectional SEM image [Figure 10D] demonstrates that the polymer region remains structurally continuous, with features extending into the NSS structure (highlighted region). The interfacial layer remained structurally continuous throughout electrochemical cycling. In contrast, the uncoated NSS sample [Supplementary Figure 5] exhibits localized protrusion-like interfacial irregularities, indicating non-uniform interfacial evolution during cycling. This comparison highlights that the polymer-coated system promotes more homogeneous interfacial contact during electrochemical operation. The post-cycling S 2p spectrum [Figure 10E] reveals the emergence of additional sulfur-containing species, including oxidized components (SO_4^{2-}/SO_4^{2-})[39] at 168.5 eV and reduced sulfide species such as Na_2S_x (160.5 eV) and Na_2S (159.5 eV), along with Sb-S related contributions. Likewise, the F 1s spectrum [Figure 10F] shows the appearance of a component at 683.5 eV assigned to NaF, accompanied by residual CF_3-related signals. These results indicate that chemical transformations of the NaTFSI salt and sulfur-containing species occur during cycling, leading to the formation of inorganic interfacial products. Overall, the combined SEM and XPS results demonstrate that the polymer-coated system maintains a continuous interfacial structure while undergoing gradual chemical evolution that produces species such as NaF and sodium sulfides[39-41]. These observations are consistent with improved interfacial stability during cycling compared with the uncoated NSS system.

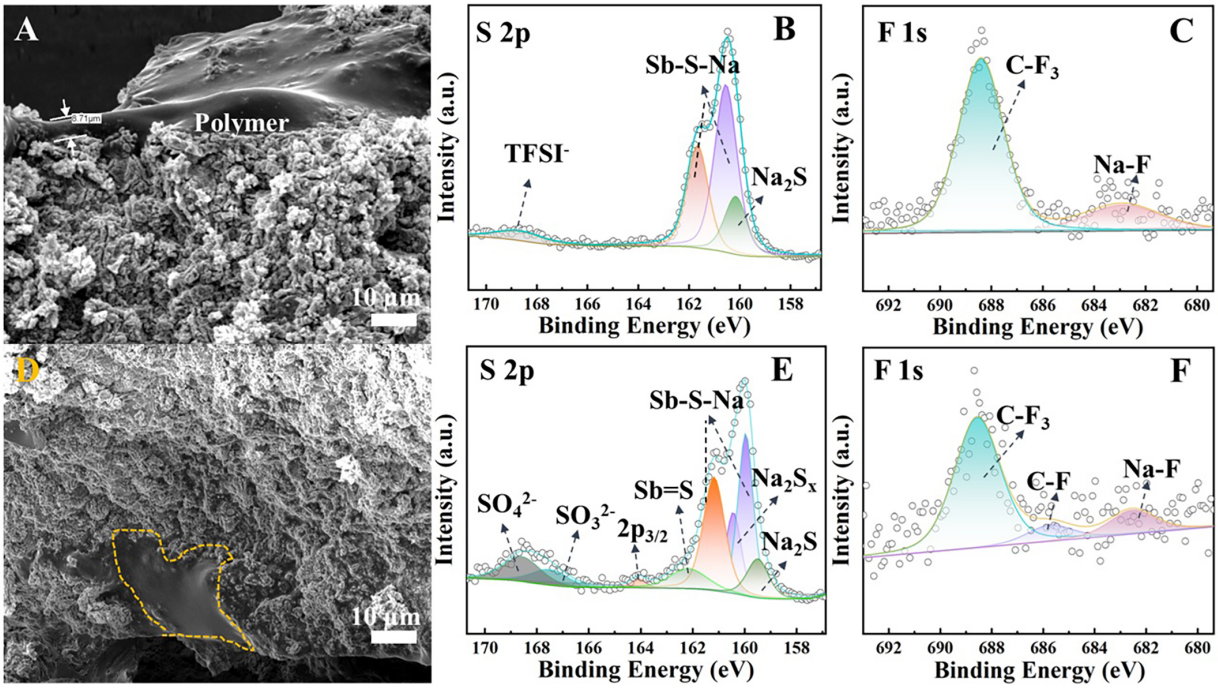

Figure 10. Cross-sectional SEM images and XPS spectra of the 7 μL AAM950-coated NSS electrolyte before and after electrochemical cycling. (A) Cross-sectional SEM image before cycling and (D) after 50 cycles. (B and C) S 2p and F 1s spectra before cycling. (E and F) S 2p and F 1s spectra after 50 cycles obtained from disassembled NFMO|7 μL AAM950-NSS-AAM950|Na cells operated at 55 °C.

The interfacial mechanism of the 7 μL AAM950-NaTFSI polymer coating on the Na_3SbS_4 solid electrolyte is illustrated in Figure 11. As shown in Figure 11A, direct contact between bare Na_3SbS_4 and sodium metal may induce interfacial reactions, leading to the formation of Na-Sb species, Na_2S, and Sb-related products that can contribute to electronic leakage and interfacial instability[27]. These processes are further associated with non-uniform Na deposition and localized penetration into the porous electrolyte structure. By comparison, Figure 11B illustrates that the polymer coating functions as an artificial interfacial layer that partially fills surface pores and improves physical contact at the electrolyte/electrode interface. Consequently, localized Na penetration into the porous structure is reduced, and more uniform Na^+ transport is promoted, consistent with the enhanced cycling stability observed in this study. XPS analysis further suggests the formation of interfacial species such as Na_2O, NaF, and Na_2S during cycling. However, the current evidence remains indirect, and therefore, the formation of a fully stabilized solid electrolyte interphase (SEI) is inferred rather than directly confirmed.

At the operating temperature of 55 °C, the polymer matrix exhibits reduced viscosity, thereby facilitating Na^+ transport across the interface and supporting stable electrochemical performance under the tested conditions. Overall, the improved electrochemical behavior is mainly associated with stabilized interfacial contact and moderated interfacial degradation enabled by the polymer layer.

The Na||NFMO cell employing the AAM950-coated NSS electrolyte delivered moderate specific capacities within the operating voltage window of the NFMO cathode (2.0-3.8 V). Direct comparison with previously reported systems employing FeS_2 or TiS_2 cathodes should be interpreted cautiously because those cathode materials typically operate within lower voltage ranges (e.g., 0.9-2.5 V), which can result in higher charge capacities under similar current conditions. To ensure a fair comparison, the current densities reported in the literature were recalculated to A g^{-1} based on the electrode thickness and mass loading provided in the original studies. As summarized in Figure 12 and Table 3[21,25,28,29,42,43], the AAM950-coated NSS system

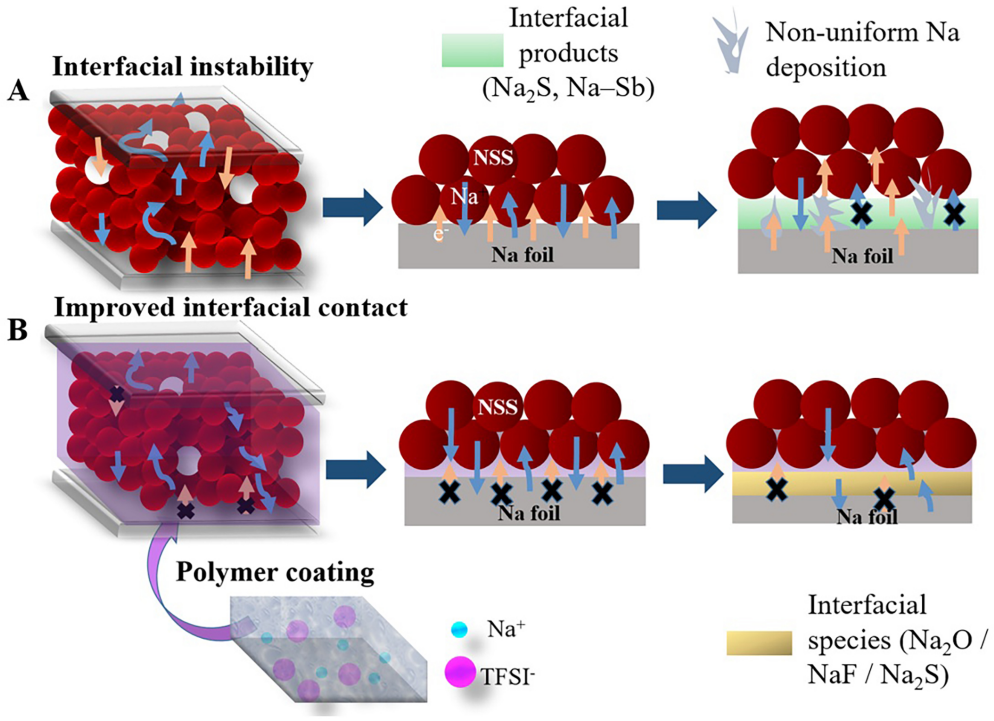

Figure 11. Schematic illustration of interfacial evolution in NSS electrolytes with and without polymer coating during cycling.

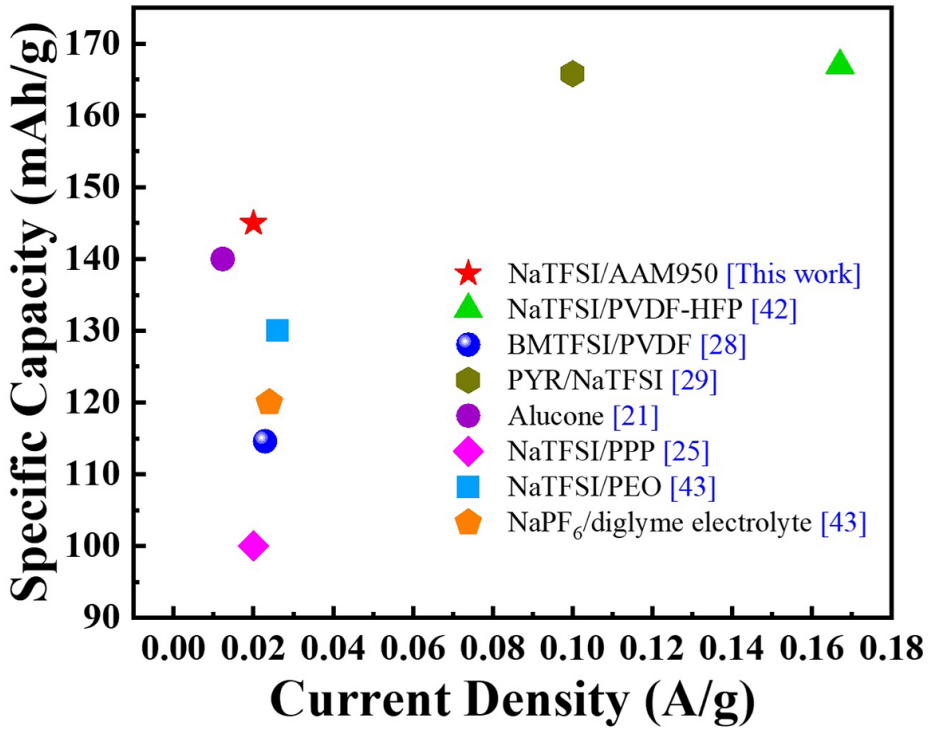

Figure 12. Comparison of charge capacities reported for Na_3SbS_4-based solid electrolytes with various surface-coating strategies from the literature and present work (AAM950/NaTFSI). Current densities were unified in A g^{-1} for consistent evaluation.

demonstrates competitive performance relative to prior reports, particularly when considering its operation at a higher voltage window.

Table 3. Comparison of the electrochemical performance of the present AAM950-coated NSS system with previously reported sodium all-solid-state battery systems

Polymer on Na_3SbS_4 pellet	Electrodes	Current density (mA g^{-1})	Charge capacity (mAh g^{-1})	Cycle number/°C	References
NaTFSI/AAM950	NFMO/Na	*0.02	149.7	50/55	This work
NaTFSI/PVDF-HFP	#TiS_2/Na	$1	167	100/RT	[42]
PVDF-0.2IL BMTFSI	NVP/Na	$0.2	114.6	400/50	[28]
(PYR/Na)TFSI	FeS_2/Na	100	165.8	300/RT	[29]
Alucone	#TiS_2/Na-mld 150C	&0.11	140	30/RT	[21]
PPP/NaTFSI	TiS_2/Na	20	100	300/50	[25]
PEO/NaTFSI	PTCDA/Na	$0.2	130	200/45	[43]
1M $NaPF_6$/diglyme electrolyte	PTCDA/ Na	$0.2	120	60/RT	[43]

Symbol for current densities: *A g^{-1}, $C, #CPE, &mA cm^{-2}. PPP: PEG-PPG-PEG; $NaPF_6$: Sodium hexafluorophosphate; NVP: $Na_3V_2(PO_4)_3$, PTCDA: perylene-3,4,9,10-tetracarboxylic dianhydride; NaTFSI: sodium bis(trifluoromethylsulfonyl)imide; RT: room temperature.

CONCLUSIONS

An artificial interfacial layer based on a 7 μL AAM950-NaTFSI polymer coating was successfully introduced onto the Na_3SbS_4 solid electrolyte to mitigate interfacial instability associated with sulfide electrolyte decomposition and non-uniform Na deposition. The conformal polymer layer partially filled surface pores and improved solid-solid contact at the electrode/electrolyte interface, leading to more stable electrochemical behavior during cycling. Although the polymer coating did not significantly enhance the intrinsic bulk ionic conductivity of NSS, it effectively stabilized the interfacial region and reduced localized degradation during repeated Na plating/stripping. As a result, the polymer-modified system delivered a discharge capacity of 137 mAh g^{-1} compared with 83.59 mAh g^{-1} for pristine NSS, together with a capacity retention of 89.6% and an average Coulombic efficiency of 99.56% over 50 cycles at 0.02 A g^{-1} and 55 °C. The combined electrochemical and interfacial analyses indicate that the improved cycling performance mainly originates from enhanced interfacial regulation and more homogeneous Na^+ transport across the solid-solid interface. Therefore, this interfacial coating strategy provides an effective approach for improving the practical stability of sulfide-based sodium all-solid-state batteries.

DECLARATIONS

Authors' contributions

Paper writing and experimental, data analysis: Thairiyarayar, C. B.
Polymer preparation and review: Wang, F. M.
Normal analyses: Kheawhom, S.; Chang, J. K.
Core idea, data analysis, and Supervision: Liu, W. R.

Availability of data and materials

The original contributions presented in this study are included in the article/Supplementary Materials. Further inquiries can be directed to the corresponding author(s).

AI and AI-assisted tools Statement

During the preparation of this manuscript, the AI tools ChatGPT Plus (OpenAI), Grammarly Free, and Nano Banna AI Pro were used solely for language editing, proofreading, and visualization enhancement. Nano Banna AI Pro was used to improve image clarity and convert SEM images into 3D visualizations for the Table of Contents graphic. ChatGPT Plus was used for language refinement and sentence rephrasing, including improvement of the polymer-related discussion, while Grammarly Free was used for grammar correction and proofreading. These tools did not influence the study design, data collection, analysis,

interpretation, or the scientific content of the work. All authors take full responsibility for the accuracy, integrity, and final content of the manuscript.

Financial support and sponsorship

The authors gratefully acknowledged the National Science and Technology Council (NSTC) project grant no. NSTC 114-2221-E-033-008, 113-2218-E-007-015, 114-2923-E-033 -001-MY3, 113-2622-E-033-003, 113-2923-E-006-002, 113-2112-M-008 -033 and 114-2112-M-008-026. The authors also appreciate the financial support from CYCU-WIArk-250CH (Wisdom Innovation Ark).

Conflicts of interest

All authors declared that there are no conflicts of interest.

Ethical approval and consent to participate

Not applicable.

Consent for publication

Not applicable.

Supplementary Materials

Supplementary Materials

REFERENCES

1. Li, Z.; Zhang, Y.; Bai, J.; Wang, J.; Zhao, H. Well-dispersed FeP@C nanoparticles anchored on MXene conductive network as outstanding cyclic performance anode for Li/Na-ion batteries. *Carbon* **2025**, *234*, 120008. DOI
2. Liu, C.; Zhang, Z.; Liao, H.; et al. Unlocking the potential: $Na_4Fe_3(PO_4)_2(P_2O_7)$ supporting the innovation of commercial sodium-ion batteries. *Adv. Funct. Mater.* **2025**, *35*, 2424759. DOI
3. Zhao, L.; Zhang, T.; Li, W.; et al. Engineering of sodium-ion batteries: opportunities and challenges. *Engineering* **2023**, *24*, 172-83. DOI
4. Yu, Z.; Shang, S. L.; Seo, J. H.; et al. Exceptionally high ionic conductivity in $Na_3P_{0.62}As_{0.38}S_4$ with improved moisture stability for solid-state sodium-ion batteries. *Adv. Mater.* **2017**, *29*, 1605561. DOI
5. Tsuji, F.; Nasu, A.; Hotehama, C.; Sakuda, A.; Tatsumisago, M.; Hayashi, A. Preparation and characterization of sodium-ion conductive Na_3BS_3 glass and glass-ceramic electrolytes. *Mater. Adv.* **2021**, *2*, 1676-82. DOI
6. Takeuchi, S.; Suzuki, K.; Hirayama, M.; Kanno, R. Sodium superionic conduction in tetragonal Na_3PS_4. *J. Solid. State. Chem.* **2018**, *265*, 353-8. DOI
7. Zhang, D.; Cao, X.; Xu, D.; et al. Synthesis of cubic Na_3SbS_4 solid electrolyte with enhanced ion transport for all-solid-state sodium-ion batteries. *Electrochim. Acta.* **2018**, *259*, 100-9. DOI
8. Huang, J.; Wu, K.; Xu, G.; Wu, M.; Dou, S.; Wu, C. Recent progress and strategic perspectives of inorganic solid electrolytes: fundamentals, modifications, and applications in sodium metal batteries. *Chem. Soc. Rev.* **2023**, *52*, 4933-95. DOI
9. Matios, E.; Wang, H.; Wang, C.; Li, W. Enabling safe sodium metal batteries by solid electrolyte interphase engineering: a review. *Ind. Eng. Chem. Res.* **2019**, *58*, 9758-80. DOI
10. Singh, R.; Tushar; Sasikumar Kala, V.; et al. Unveiling the importance of solid-liquid interphase for the development of all solid-state sodium metal batteries. *Batter. Supercaps.* **2025**, *8*, e202500408. DOI
11. Lacivita, V.; Wang, Y.; Bo, S.; Ceder, G. *Ab initio* investigation of the stability of electrolyte/electrode interfaces in all-solid-state Na batteries. *J. Mater. Chem. A.* **2019**, *7*, 8144-55. DOI
12. Wu, M.; Liu, H.; Qi, X.; et al. Structure designing, interface engineering, and application prospects for sodium-ion inorganic solid electrolytes. *InfoMat* **2024**, *6*, e12606. DOI
13. Wenzel, S.; Leichtweiss, T.; Weber, D. A.; Sann, J.; Zeier, W. G.; Janek, J. Interfacial reactivity benchmarking of the sodium ion conductors Na_3PS_4 and sodium β-alumina for protected sodium metal anodes and sodium all-solid-state batteries. *ACS. Appl. Mater. Interfaces.* **2016**, *8*, 28216-24. DOI PubMed
14. Xie, G.; Tang, M.; Xu, S.; Brown, A.; Sang, L. Degradation at the Na_3SbS_4/anode interface in an operating all-solid-state sodium battery. *ACS. Appl. Mater. Interfaces.* **2022**, *14*, 48705-14. DOI

15. Tian, Y.; Sun, Y.; Hannah, D. C.; et al. Reactivity-guided interface design in na metal solid-state batteries. *Joule* **2019**, *3*, 1037-50. DOI
16. Moeez, I.; Susanto, D.; Chang, W.; Lim, H.; Chung, K. Y. Artificial cathode electrolyte interphase by functional additives toward long-life sodium-ion batteries. *Chem. Eng. J.* **2021**, *425*, 130547. DOI
17. Moorthy, M.; Thangavel, R.; Krishnan Ganesan, B.; Saha, A.; Hong, S.; Lee, Y. Ultra-high areal capacity, ultra-long life, dendrite-free sodium metal anode enabled by antimony-based Na-ion conducting artificial SEI layers. *Chem. Eng. J.* **2024**, *498*, 155234. DOI
18. Yihao, G. U. O.; Xiaoyu, H. U.; Yongfeng, Y. U. A. N. Dual-site doping of tungsten and fluorine enhances the interface stability of Na_3SbS_4 in all-solid-state sodium metal batteries. *J. Mater. Sci.* **2025**, *43*, 1673-2812. DOI
19. Wang, L.; Liu, G.; Li, Y.; Weng, W.; Xin, X.; Yao, X. Tungsten and boron codoping toward high ionic conductivity and stable sodium solid electrolyte for all-solid-state sodium batteries. *ACS. Appl. Mater. Interfaces.* **2024**, *16*, 4847-53. DOI
20. Zhang, Z.; Cao, H.; Zhang, L. Preparation and electrochemical properties of ionic-liquid-modified Na3SbS4 membrane composite electrolytes. *J. Mater. Sci.* **2021**, *56*, 10565-74. DOI
21. Zhang, S.; Zhao, Y.; Zhao, F.; et al. Gradiently sodiated alucone as an interfacial stabilizing strategy for solid-state Na metal batteries. *Adv. Funct. Mater.* **2020**, *30*, 2001118. DOI
22. Ren, Y.; Hortance, N.; Mcbride, J.; Hatzell, K. B. Sodium-Sulfur batteries enabled by a protected inorganic/organic hybrid solid electrolyte. *ACS. Energy. Lett.* **2020**, *6*, 345-53. DOI
23. Wang, T.; Yu, Q.; Li, Z.; et al. The potential of solid-state potassium-ion batteries with polymer-based electrolytes. *Carbon. Energy.* **2025**, *7*, e670. DOI
24. Chen, S.; Che, H.; Feng, F.; et al. Poly(vinylene carbonate)-based composite polymer electrolyte with enhanced interfacial stability to realize high-performance room-temperature solid-state sodium batteries. *ACS. Appl. Mater. Interfaces.* **2019**, *11*, 43056-65. DOI
25. Li, Y.; Arnold, W.; Halacoglu, S.; Jasinski, J. B.; Druffel, T.; Wang, H. Phase-transition interlayer enables high-performance solid-state sodium batteries with sulfide solid electrolyte. *Adv. Funct. Mater.* **2021**, *31*, 2101636. DOI
26. Zhang, Y.; Hu, P.; Yao, Y. Polymer-sulfide composite solid state electrolyte with enhanced interfacial stability with sodium metal. *Meet. Abstr.* **2017**, *MA2017-01*, 559. DOI
27. Hu, P.; Zhang, Y.; Chi, X.; et al. Stabilizing the interface between sodium metal anode and sulfide-based solid-state electrolyte with an electron-blocking interlayer. *ACS. Appl. Mater. Interfaces.* **2019**, *11*, 9672-8. DOI
28. Wang, Z.; Zhang, L.; Shang, X.; et al. Enhanced electrochemical performance enabled by ionic-liquid-coated Na_3SbS_4 electrolyte encapsulated in flexible filtration membrane. *Chem. Eng. J.* **2022**, *428*, 132094. DOI
29. Li, Y.; Halacoglu, S.; Shreyas, V.; et al. Highly efficient interface stabilization for ambient-temperature quasi-solid-state sodium metal batteries. *Chem. Eng. J.* **2022**, *434*, 134679. DOI
30. Wang, F.; Wan, C.; Wang, Y. Synthesis of functionalized copolymer electrolytes based on polysiloxane and analysis of their conductivity. *J. Appl. Electrochem.* **2008**, *39*, 253-60. DOI
31. Thairiyarayar, C. B.; Huang, C.; Gandomi, Y. A.; Hsieh, C.; Liu, W. Synthesis and characterization of Na_3SbS_4 solid electrolytes via mechanochemical and sintered solid-state reactions: a comparative study. *Sustainability* **2023**, *15*, 15662. DOI
32. Wang, H.; Chen, Y.; Hood, Z. D.; et al. An air-stable Na_3SbS_4 superionic conductor prepared by a rapid and economic synthetic procedure. *Angew. Chem. Int. Ed.* **2016**, *128*, 8693-7. DOI
33. Tang, B.; Zhao, Y.; Wang, Z.; et al. Ultrathin salt-free polymer-in-ceramic electrolyte for solid-state sodium batteries. *eScience* **2021**, *1*, 194-202. DOI
34. Kmiec, S.; Ruoff, E.; Darga, J.; Bodratti, A.; Manthiram, A. Scalable glass-fiber-polymer composite solid electrolytes for solid-state sodium-metal batteries. *ACS. Appl. Mater. Interfaces.* **2023**, *15*, 20946-57. DOI PubMed
35. Mikenda, W.; Preisinger, A. Vibrational spectra of Na_3SbS_4, $Na_3SbS_4{\cdot}9H_2O$ (Schlippe's salt) and $Na_3SbS_4{\cdot}9D_2O$. *Spectrochim. Acta. A. Mol. Biomol. Spectrosc.* **1980**, *36*, 365-70. DOI
36. Noor, S.; Su, N.; Khoon, L.; et al. Properties of high Na-ion content N-propyl-N-methylpyrrolidinium bis(fluorosulfonyl)imide -ethylene carbonate electrolytes. *Electrochim. Acta.* **2017**, *247*, 983-93. DOI
37. Khurana, S.; Chandra, A. Ionic liquid-based organic-inorganic hybrid electrolytes: impact of in situ obtained and dispersed silica. *J. Polym. Sci. B. Polym. Phys.* **2017**, *56*, 207-18. DOI
38. Wang, W.; Ding, M.; Chen, S.; et al. A novel composite solid electrolyte with ultrahigh ion transference number and stability for solid-state sodium metal batteries. *Chem. Eng. J.* **2024**, *491*, 151989. DOI
39. Liu, Y.; Lu, S.; Weng, S.; et al. Interphase-regulated room-temperature sodium-sulfur batteries enabled by a nonflammable dual-functional electrolyte. *Adv. Energy. Mater.* **2024**, *15*, 2404890. DOI
40. Eshetu, G. G.; Diemant, T.; Hekmatfar, M.; et al. Impact of the electrolyte salt anion on the solid electrolyte interphase formation in sodium ion batteries. *Nano. Energy.* **2019**, *55*, 327-40. DOI

41. Miao, Y.; Lin, D.; Liu, J.; et al. A non-fluorinated, weakly solvating electrolyte for efficient sodium-sulfurized polyacrylonitrile batteries. *J. Mater. Chem. A.* **2025**, *13*, 17479-88. DOI
42. Mwemezi, M.; Park, W. B.; Ikhe, A. B. Improvement of interfacial stability between Na metal and Na_3PS_4 family solid electrolyte for all-solid-state sodium metal batteries. *Electrochim. Acta.* **2024**, *480*, 143919. DOI
43. Lu, Y.; Li, L.; Zhang, Q.; Cai, Y.; Ni, Y.; Chen, J. High-performance all-solid-state electrolyte for sodium batteries enabled by the interaction between the anion in salt and Na_3SbS_4. *Chem. Sci.* **2022**, *13*, 3416-23. DOI PubMed PMC